UNIVERSITEIT VAN PRETORIA
UNIVERSITY OF PRETORIA
YUNIBESITHI YA PRETORIA

# The influence of sputtering on ion implantation profiles

by

Samuel Jaye Thugwane

Submitted in partial fulfillment of the requirements for the degree Master of Science

in the

Faculty of Science (Department of Physics)
University of Pretoria
Pretoria

DECEMBER 11, 2000

Supervisor: Prof. E. Friedland

Co-supervisor: Dr. M. Hayes

© University of Pretoria

# SUMMARY

The accurate knowledge of the implantation profiles is of considerable interest for testing theoretical models on the stopping of ions in matter, as well as for many important applications in metallurgy and semiconductor technology. Measurements of the depth distribution profiles of the implanted ions provide information on a wide range of fields, including ion-solid interactions, doping and diffusion.

Several experimental methods have been employed to determine the depth distributions of the implanted ions. They can be divided into destructive and non-destructive methods. Most experimental results found in the literature are for heavier ions implanted into lighter target materials where the non-destructive Rutherford Back-scattering method can be employed. Nuclear Reaction Analysis also provides a non-destructive method for determining the implanted profile of impurity atoms with mass number smaller or similar to that of the target material.

One of the important effects in ion implantation is sputtering, the process in which the surface of the target material is eroded due to ion bombardment. This process modifies range moments of implantation profiles for high fluences. This study is mainly concerned about effects of sputtering on the implanted depth profile as a function of fluence and target mass. Sputtering correction factors are determined numerically to correct the theoretical depth distributions.

# ACKNOWLEDGEMENTS

I would like to thank the following persons for their help in this present work.

My supervisor, Prof. Erich Friedland who guided me throughout this study.

Dr. Michael Hayes my co-supervisor, his experimental data was analysed in this study.

Mr. Julius Madonsela, for the fruitful discussions we had and his encouragement.

My dear mom who gave me support since I started my education till thus far, thanks God, for giving me such a loving mom.

The financial assistance of the University of Pretoria and National Research Foundation (NRF) is greatfully acknowledged.

# TABLE OF CONTENTS

1. INTRODUCTION 6
2. THE STOPPING OF IONS IN SOLIDS 9
2.1 Energy loss 9
2.2. Energy dependence of the stopping power 12
2.2.1 Electronic stopping power 13
2.2.2 Nuclear stopping power 15
2.3 Energy straggling 18
2.4 Range distribution 19

3. SPUTTERING 22
3.1 Collision cascade 22
3.2 The Sigmund model 24
3.2.1 The nuclear stopping power 26
3.2.2 The α-factor 27
3.2.3 The surface binding energy 29

4. NUCLEAR REACTION ANALYSIS 31
4.1 Nuclear reaction 32
4.2 Resonance reaction 34

5 METHOD OF SPUTTERING CORRECTION OF IMPLANTED IMPURITY PROFILES IN METALS 37
5.1 Assumptions of the method 37
5.2 Description of method 38

5.3 Calculations 38
5.4 Sputtering corrections 39
5.5 Testing of the method 41
5.5.1 Gaussian aproximation 41
5.5.2 Comparison of the numerical and the analytical methods 43
5.6. Application of the sputtering correction method 46
5.6.1 Depth profile dependence on the sputtering yield 46
5.6.2 Depth profile dependence on the fluence 48
5.7. The retained dose 50

6. ANALYSIS OF EXPERIMENTAL IMPLANTATION PROFILES

6.1 Aluminium implanted into different targets 52
6.1.1 Aluminium implanted into vanadium 54
6.1.2 Aluminium implanted into chromium 55
6.1.3 Aluminium implanted into cobalt 56
6.1.4 Aluminium implanted into yttrium 57
6.1.5 Aluminium implanted into platinum 58
6.1.6 Aluminium implanted into manganese 59
6.1.7 Aluminium implanted into tantalum 60
6.1.8 Aluminium implanted into tungsten 62
6.1.9 Aluminium implanted into hafnium 63
6.2 Comparison with the results in the literature 64
6.3 Conclusion 65

REFERENCES 66
APPENDIX A: Computer code of sputtering corrections 69

# CHAPTER 1

# INTRODUCTION

Ion implantation is becoming an increasingly important technique for introducing one material into the near surface regions of another material. In essence the entire problem is to decide which chemical, electrical, mechanical or optical properties are required in an area of the surface, then to choose the appropriate ion species which will achieve these results. A judicious choice of injection energies and masks will then allow the implanted impurities to determine the depth and spatial shape of the modified layers [1]. It also has an advantage over diffusion method, that both the uniformity and depth distribution can be accurately controlled and the final result can be quite independent of factors such as surface chemistry and solid solubility.

The accurate knowledge of implanted profiles is of considerable interest for testing theoretical models on the stopping of ions in matter, as well as for many important applications in metallurgy and semiconductor technology [2]. When an energetic ion or atom enters the target material, it loses energy via two independent processes, namely, nuclear energy loss and electronic energy loss. The former is related to energy loss by the incident ion through elastic interaction with the target atoms and the latter is related to energy transfer to electrons of the atomic shell. The stopping of ions in solids is discussed in Chapter 2.

One of the effects usually neglected in ion implantation is sputtering [3]. For shallow devices, however, low energies and high doses have to be used to obtain the desired junction depth and sheet resistivity. In this case, sputtering has to be considered. This reduces the projected range of the depth distribution profiles to some extent such that correction factors must be employed. Chapter 3 explains this process in full details.

Several experimental techniques have been developed in order to determine the depth distributions of the implanted ions. There are destructive and non-destructive techniques. In destructive techniques the surface of the sample is removed by either etching or ion sputtering, which in turn damage the target material. The profiles are obtained by Auger-electron spectroscopy or secondary ion mass spectroscopy. On the other hand non-destructive techniques such as Rutherford Backscattering (RBS), rely on the elastic interaction of incident light ions with the atomic nuclei of the target. For heavy atoms in light mass targets the RBS technique provides the actual implanted profile of the impurity atoms in the target. One of the drawbacks of RBS technique is the low detection sensitivity of light mass elements and the strong background from heavy substrate materials [4]. It is more suitable for impurity atoms (of mass $M_1$) heavier than substrate material (of mass $M_2$), i.e $M_1 > M_2$.

One of the useful non-destructive techniques for light impurities in heavy targets is Nuclear Reaction Analysis (NRA). The procedures used in this technique are similar to those for the RBS measurements. It provides a non-destructive method for determining the implantation profiles of impurity atoms with a mass number smaller or similar to that of the target material.

Strong resonances are needed for this technique, which are not available for all cases. Therefore the experimental results for light ion implantations are relatively scarce. Most results are obtained by means of (p,γ) resonances [5-7], which for example occur with sufficiently large cross sections at proton energies in $^{13}C$, $^{15}N$, $^{27}Al$. Especially the strong 992 keV resonance in $^{27}Al$ with a width of only 100 eV [8] is very useful for depth profiling and therefore a relatively large body of data for implantation profiles of aluminium is available. NRA is discussed in detail in Chapter 4.

Chapter 5 deals with the sputtering correction method developed to account for the sputtering effects that occurs during ion implantation, which leads to the modification of range moments. The theoretical depth profiles were used in this study in order to observe how they are affected by sputtering. A computer program was written to correct these theoretical depth profiles for sputtering. Range moments are determined from these theoretical depth profiles before and after correction for sputtering. Then the sputtering correction factors were calculated as the ratio of the range moments for the corrected and the uncorrected theoretical depth profiles. These calculated correction factors are used to correct the experimental results.

Results are discussed in Chapter 6 and references are listed at the end. Appendix A shows the computer program used.

UNIVERSITEIT VAN PRETORIA
UNIVERSITY OF PRETORIA
YUNIBESITHI YA PRETORIA

# CHAPTER 2

# THE STOPPING AND RANGE OF IONS IN SOLIDS

The stopping of energetic ions in matter has been a subject that has received great theoretical and experimental interest for many years. The theoretical treatment of the stopping of ions in matter is due greatly to the work of Bohr, Bethe, Bloch, Firsov and Lindhard as discussed in [4]. The theory has achieved a remarkable progress and at present we have analytical solutions as well as Monte–Carlo type simulations permitting the calculation of ranges and range parameters for any ion-solid system. From the experimental side, the reasons for the large growth in the field are the great development in ion implantation technology and in ion beam analytical methods like Rutherford back scattering (RBS) and nuclear reaction analysis (NRA).

The accurate knowledge of the final distribution of implanted ions in solids has far reaching implications in such diverse fields as impurity doping in semiconductors, dosimetry and detector design, radiation therapy, modification of tribological properties of solids.

## 2.1 ENERGY LOSS MECHANISMS

A projectile incident on a target will suffer a series of discrete collision events that slow it down and transfers energy to the substrate. The major

processes of energy loss are (i) elastic direct collisions between the projectile ion and a screened nucleus of the target, (ii) excitation of electrons in bound state and (iii) charge exchange processes between the ion and atoms of the solid. These three processes are illustrated in figure 2.1. Each process is energy dependent and so each makes different contributions to energy losses along the path. These processes may be treated independently and we may write a differential energy loss equation as:

$$dE/dx = (dE/dx)_{\text{nuclear}} + (dE/dx)_{\text{electronic}} + (dE/dx)_{\text{exchange}} \qquad (2.1)$$

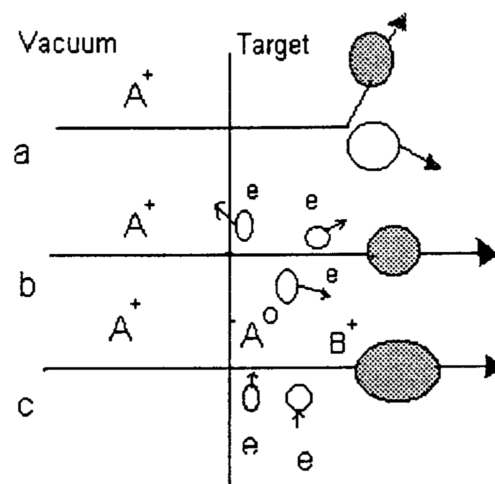


**Figure 2.1:** Fundamental processes of energy loss, (a) Elastic atomic collision, (b) inelastic electronic collisions, (c) charge exchange collision.

The differential function is known as the stopping power (energy loss per unit path-length) or specific energy loss. It is often given the symbol $n_0S$ [9]. The exchange component to energy loss is related to pick up or loss of electrons by the projectile as it traverses the target. For light particles

moving at high energies this process can be neglected and the rate of energy loss can be expressed as a combination of the nuclear and the electronic stopping powers.

$$dE/dx = n_0[S_e(E) + S_n(E)] \qquad (2.2)$$

where $S_e$ and $S_n$ are electronic and nuclear energy loss cross sections and $n_0$ is the atomic density.

The nuclear energy loss may be modelled by collision between the ion and a screened nucleus of the target. The nuclear stopping power increases with energy and reaches a maximum at low energies as illustrated in figure 2.2. Nuclear stopping is very important in its effect on the target material since it may involve substantial transfer of energy to target atoms which then recoil through the target material and themselves suffer more collisions and lose more energy. Such secondary recoil atoms will end up displaced from their original lattice position. Target atoms located at or close to the surface may receive sufficient momentum to be ejected into space leading to surface erosion or sputtering.

Electronic energy loss is due to inelastic collisions of the projectile ion with the electrons of the target. The energy loss by electronic collisions increases with energy and reaches a maximum only at high energies when the projectile interaction time becomes less than the response time of the target electrons. In general, for particles with high velocities the electronic energy loss rate exceeds that for nuclear collisions. Projectile direction is not significantly altered by electronic collisions because projectile mass greatly

exceeds that of the electron. The transferred energy results in the excitation and ionization of the target atoms.

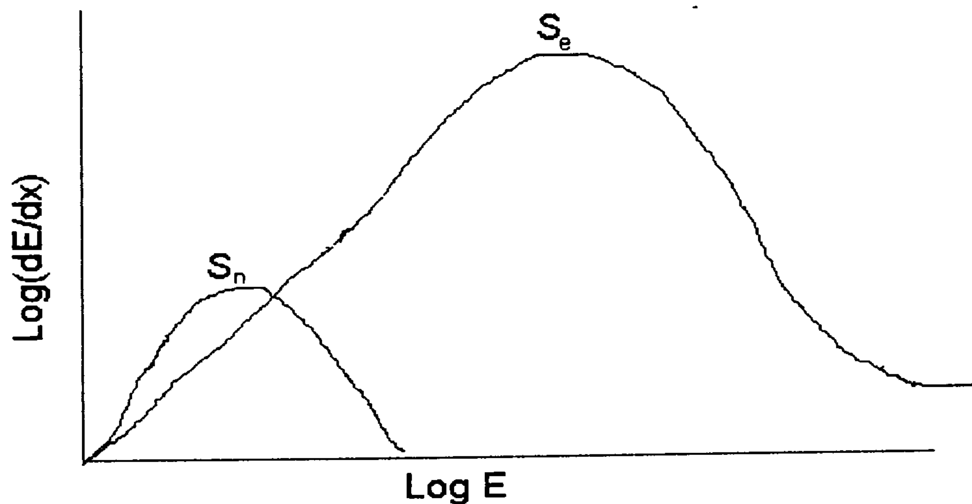


**Figure 2.2:** General form of specific energy loss as function of energy for the nuclear and electronic stopping.

## 2.2 THE DEPENDENCE OF THE STOPPING POWERS ON THE ENERGY

In the low energy region (keV) the nuclear and the electronic stopping powers compete. Nuclear stopping dominates at very low energies, but at higher energies (MeV) the electronic stopping power dominates. The criterion of separating the energy regions is the velocity of the projectile relative to the orbital velocity of the atomic or molecular electrons in the outermost shell or subshell of a given target atom [10]. When the projectile

velocity v is much greater than that of an orbital electron, electronic stopping dominates, i.e.where

$$v > v_0 Z_2^{\ 2/3} \tag{2.3}$$

and $v_0$ is the Bohr velocity

$$v_0 = e^2/h = 2.188 \times 10^6 \text{ m/s} \tag{2.4}$$

where $Z_2$ is the atomic number of the target atom, $e$ is the electron charge and $h$ is Planck's constant.

### 2.2.1 ELECTRONIC STOPPING

The low energy region ($v < v_0 Z_2^{\ 2/3}$) was first investigated by Lindhard and Winter [11]. They assumed that the electrons form a free electron gas, and were able to demonstrate that the electronic stopping cross section is proportional to the velocity of the ions, and therefore proportional to the root of the energy:

$$S_e(E) = -1/n_0(dE/dx)_e = -k`E^{\,½} \tag{2.5}$$

where

$$k` = kC_R/[(C_E^{\,½})n_0] \tag{2.6}$$

and

$$k = \xi_e 0.0793 Z_1^{\frac{1}{2}} Z_2^{\frac{1}{2}} \frac{(M_1+M_2)^{\frac{3}{2}}}{[(Z_1^{\frac{2}{3}}+Z_2^{\frac{2}{3}})^{\frac{3}{4}} M_1^{\frac{3}{2}} M_2^{\frac{1}{2}}]} \qquad (2.7)$$

where $Z_1$ is the atomic number of the incident ion, $M_1$ and $M_2$ are atomic masses of the incident ion and target respectively, $\xi_e$ is a dimensionless constant of the magnitude $Z_1^{1/6}$; $C_R$ and $C_E$ are obtained from the reduced range $\rho$ and reduced energy $\varepsilon$ given by the following relations respectively,

$$\rho = C_R R = 4\pi a^2 n_o M_1 M_2 R/(M_1+M_2)^2 \qquad (2.8)$$

and

$$\varepsilon = C_E E = a M_2 E/[Z_1 Z_2 e^2 (M_1 + M_2)] \qquad (2.9)$$

where $a$ is the Biersach screening radius defined as follows

$$a = 0.885 a_o/(Z_1^{0.23} + Z_2^{0.23}) \qquad (2.10)$$

$n_o$ is the atomic density and $a_0$ = 0.0529 angstroms is the Bohr radius. The $R$ and $E$ stand for the range and energy respectively and k is the proportionality constant in the reduced representation, i.e.,

$$-(d\varepsilon/d\rho)_e = k\varepsilon^{1/2} \qquad (2.11)$$

The values of $k$ are generally between 0.1 and 0.25.This equation above is valid for ion velocities below the value:

$$v < Z_2^{2/3} v_0 \tag{2.12}$$

For higher energies ($v > v_0 Z_2^{2/3}$) the stopping power is well described by the Bethe–Bloch formalism. In this region the electronic stopping power decreases with increase in energy. This is due to the fact that the higher the velocity of the incident ion the less time it has to interact with each target atom it comes into contact. The formula that describes stopping in the Bethe-Bloch formalism is [12]:

$$S_e = (4\pi e^4 Z_1^2 Z_2^2 / m v^2)[\ln (2mv^2/I) + \ln (1/(1-\beta^2) - \beta^2 - C/Z_2] \tag{2.13}$$

where m is the mass of the electron, $\beta = v/c$, $v$ is the incident ion velocity, $c$ is the velocity of light, $I$ is the mean excitation potential and $C/Z_2$ describes the shell correction. The mean excitation potential $I$ for most elements is roughly $10Z_2$ in eV.

## 2.2.2 NUCLEAR STOPPING

In the very low (keV) energy region, where the particle velocity is much less than the Bohr velocity, the nuclear stopping dominates. The calculation of the nuclear stopping uses two main assumptions, simple screened Coulomb potential and the impulse approximation. The interaction potential between

two atoms $Z_1$ and $Z_2$ can be written in the form of a screened Coulomb potential

$$V(r) = Z_1 Z_2 e^2 \chi(r/a)/r, \tag{2.14}$$

In the impulse approximation the change in momentum is given by

$$\Delta p = \int F dt = 1/v \int F dx \tag{2.15}$$

where, $F$ is the component of the force acting on the ion perpendicular to its direction. Using the geometry of figure 2.3, the force may be written with $r = (x^2+b^2)^{1/2}$ as

$$F = -\partial V(r)/\partial y = -\partial V\,(x^2+b^2)^{1/2}\,/\partial b \tag{2.16}$$

The energy transferred, $T$, to the recoiling nucleus is

$$T = \Delta p^2/2M_2 \tag{2.17}$$

The cross section $d\sigma(T)$ for transfer of energy between $T$ and $T + dT$ is

$$d\sigma = -2\pi b db \tag{2.18}$$

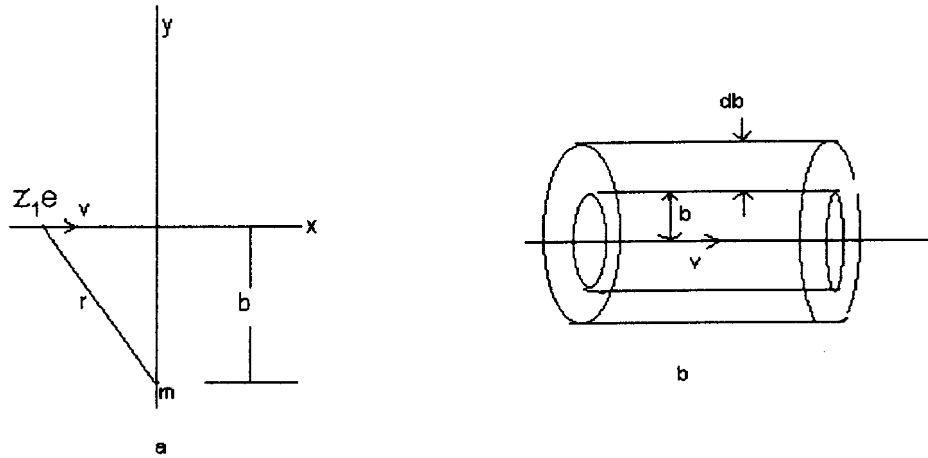


**Figure 2.3:** Shows an ion with charge $Z_1$ passing an atom at distance b.

The nuclear stopping cross section $S_n$ is given by

$$S_n = - \int T d\sigma \qquad (2.19)$$

Lindhard used a description that expresses the nuclear energy loss in terms of the reduced energy $\varepsilon$, as follows

$$(d\varepsilon/d\rho)_n = S_n(\varepsilon) \qquad (2.20)$$

so that

$$(dE/dx)_n = 4\pi a Z_1 Z_2 e^2 M_1 S_n(\varepsilon)/[(M_1+M_2)] \qquad (2.21)$$

For this study we used the by Ziegler and Biersack universal screening potential [13] which results in

$$S_n(\varepsilon) = 0.5\ln(1+1.1383\varepsilon)/[\varepsilon + 0.1321\varepsilon^{0.21226} + 0.19593\varepsilon^{0.5}] \quad (2.22)$$

## 2.3 ENERGY STRAGGLING

An energetic particle that moves through a medium loses energy via many individual encounters. Such a discrete process is subject to statistical fluctuations. As a result, identical energetic particles do not have exactly the same energy after passing through a thickness $t$ of a homogeneous medium. The energy loss $\Delta E$ is subject to fluctuations. The phenomenon is called energy straggling. Energy straggling places a finite limit on the precision with which energy losses, and hence depths can be resolved. Light particles in the MeV energy range lose energy primarily by encounters with the electrons in the target and the dominant contribution to energy straggling is due to the statistical fluctuations in these electronic interactions. Bohr derived the value for energy straggling, $\Omega_B$, for any thickness $t$, expressed by the following relation:

$$\Omega_B{}^2 = 4\pi Z_1{}^2 e^4 n_o Z_2 t \quad (2.23)$$

The energy resolution is normally composed of two contributions: instrumental resolution $\delta E_d$ and energy straggling $\delta E_s$ [10]. Assuming the two contributions are independent and satisfy Gauss' statistics, the total resolution, $\delta E_1$ is given by

$$(\delta E_1)^2 = (\delta E_d)^2 + (\delta E_s)^2 \quad (2.24)$$

The instrumental resolution is mainly determined by the beam width $\delta E_p$ and resonance width $\Gamma$, thus

$$(\delta E_d)^2 = (\delta E_p)^2 + \Gamma^2 \tag{2.25}$$

Note that the full width at half maximum is $2(2\ln 2)^{1/2}$ times the standard deviation, thus

$$\delta E_s = 2.35\Omega_B \tag{2.26}$$

Bohr's theory predicts that energy straggling does not depend on the energy of the projectile and that the value of the energy variation increases with the square root of the electron density per unit area $n_o Z_2 t$ in the target. Straggling sets a fundamental limit to the depth resolution. Since $\Omega_B^2$ is proportional to $t$, the straggling is a function of the depth penetration.

## 2.4 THE MOMENTS OF A DISTRIBUTION

From the point of view of ion implantation it is the penetration depth of the projectile that is of significance. As the projectile undergoes its various energy loss processes it eventually slows down to the point where it may be stopped by a lattice atom and thereby comes to rest at an interstitial site.

The relationship of the final location of the projectile with respect to the surface then represents penetration depth. The energy loss processes are statistically related concepts due to the fluctuations of energy loss and

angular deviation at each collision event. Thus there is not a single penetration depth but rather a distribution about an average value that we call mean range. As illustrated in figure 2.4, range may be specified in various ways depending on whether one is interested in total path length $R$ or the distance measured parallel to the original ion direction ($R_p$). Total range is readily derived from specific energy loss

$$R_{(total)} = \int_0^E \frac{dE}{dE/dx} \tag{2.27}$$

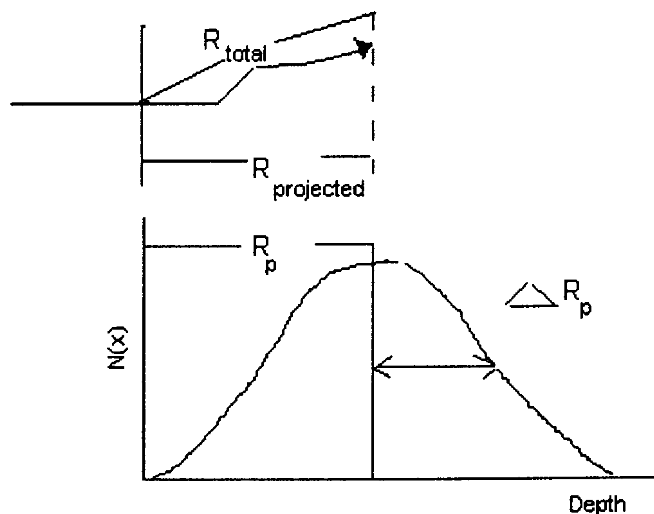


**Figure 2.4:** Range distribution is shown in this figure.

The upper integration limit, $E$, is the initial energy of the projectile impinging on the target. The lower limit of integration should be the energy at which the projectile is captured by the lattice, in practice this may be taken as zero. Projected range, a more significant parameter, is smaller than

the total range. The projected range is defined as the average distance of the implanted impurities from the surface:

$$R_p = \frac{\sum_{i=1}^{N} x_i}{N} \tag{2.28}$$

Where, $x_i$, is the distance from the surface to the position of an implanted impurity atom and N is the number of implanted impurities. The three higher moments are given by:

Straggling: $\Delta R_p = [\Sigma(x_i - R_p)^2]/N$

Skewness: $\gamma = [\Sigma(x_i - R_p)^3]/[N\Delta R_p^3]$

Kurtosis: $\beta = [\Sigma(x_i - R_p)^4]/[N\Delta R_p^4]$

The straggling is the standard deviation, skewness is a measure of the deviation from a symmetric distribution of the profile and the kurtosis indicates the flatness at the top of the profile. For a gaussian distribution $\gamma = 0$ and $\beta = 3$.



b15213249
i1576199X

# CHAPTER 3

# SPUTTERING

During ion bombardment of a target energy can be deposited near the surface at such a high rate that atoms are removed from the solid. This phenomenon of removal of surface target atoms by ion bombardment was recognized and used for technological processes long before it was understood at the atomic level. It is called sputtering. Practical use is made of the sputtering process in three major areas: namely; materials synthesis, controlled etching and surface analysis by secondary ion mass spectrometry (SIMS) and Auger Electron Spectroscopy (AES) [14].

## 3.1 COLLISION CASCADE

In the sputtering process, the incident energetic ion strikes the surface, penetrates, and undergoes a series of collisions with the atoms in the solid. As this incident ion slows down, energy in excess of the lattice binding energy (on the order of 10 eV) may be transferred to the atoms of the solid. Atoms that recoil with sufficient energy undergo secondary collisions, thereby creating another generation of recoiling atoms. Thus a collision cascade develops [15]. Some of these collisions will impart momentum to atoms of the solid in the direction of the surface. Through a chain of collisions this momentum may be transferred to atoms at the surface,

causing their ejection from the solid as neutral, positive or negative ions. Figure 3.1 below shows the ion-solid interactions and sputtering process.

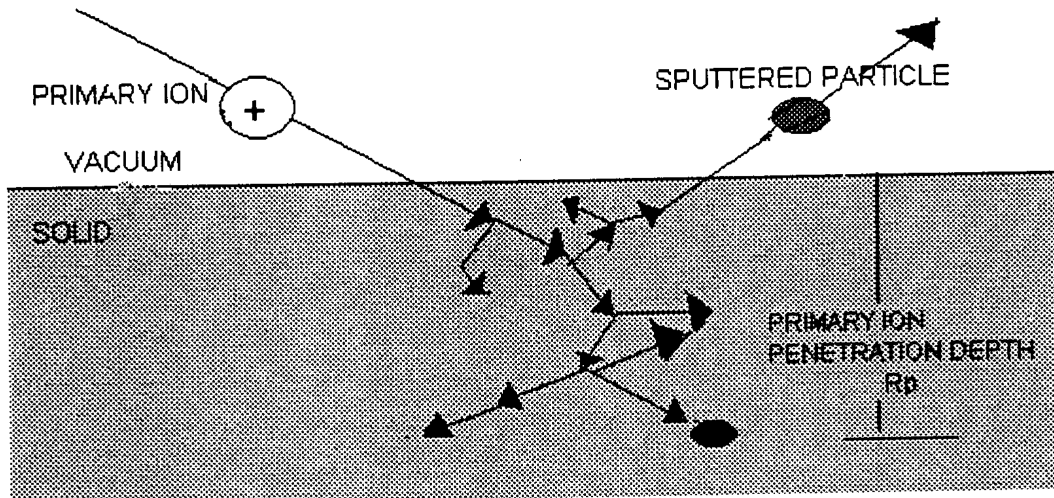


Figure 3.1.Schematic of the ion-solid interaction and sputtering process.

Collision cascade evolution is influenced by the crystal lattice structure through channeling, blocking, and focusing [16]. Depending on the energy and mass of the incident ions, three different collision cascade regimes can be identified:

1. For low energy and light-ions bombardment, the collision cascades are very dilute and involve only a few atoms. This is the so called single knock-on regime
2. Under bombardment with ions of medium or large mass at energies exceeding a few keV, the collision cascades get larger and more dense. If each target atom is at rest before is gets hit, this is called the linear cascade regime

3. With ions of high atomic number, or with molecular ions of sufficient high energy (above about 100 keV), and with target atoms of high atomic number, the cascades get very dense and target atoms may be knocked on while they are already in motion. This is called the thermal spike regime.

The erosion in sputtering is measured by the sputtering yield defined as the number of sputtered atoms per incident ion, which lies in the range of 0.5 – 20 depending upon the ion species, ion energy, and target material. Sputtering yield can be rather accurately predicted by theory for single elemental materials.

It is possible to simulate the sputtering process on a computer via a series of binary events. Due to various reasons (e.g. a proper treatment of the low energy collision cascades) many of these computer codes are inaccurate for the calculation of sputter yields. The ones that are accurate (e.g. TRIM-SP) are not readily available. The sputter problem has been approached using transport theory, which considers dynamics of the collision cascade and derives the total energy flux in the backward direction. There are many sputtering models describing various energy regions [17]. The most popular approach is by Sigmund [15] which is discussed in the next paragraph.

## 3.2 THE SIGMUND MODEL

Sigmund's theory was derived for the linear cascade regime. Sigmund used the Boltzmann transport equation to treat collision cascades. The atomic collisions (ion-target atom and target-target atoms) are assumed to be binary

between point-like objects. Furthermore, the collisions are assumed to take place between a moving and a stationary atom. This assumption linearizes the Boltzmann equation but does not hold for the thermal spike regime. The Boltzmann equation, with the surface as a boundary condition, is very difficult to solve. Therefore, Sigmund treated the target as an infinite medium with an imaginary surface plane embedded. Inelastic energy losses (ionization and excitation) are also neglected [18].

The Sigmund equation can be obtained in a semi-empirical manner [1].

$$Y = \lambda F(E) \tag{3.1}$$

The first term $\lambda$ is the parameter that contains the material properties such as surface binding energy $U_0$ and atomic density,

$$\lambda = 3/(4\pi^2 n_0 C_0 U_0) \tag{3.2}$$

and where the constant $C_0$ is given by

$$C_0 = (\pi \lambda_0 a_{BM}^2)/2 \tag{3.3}$$

The values of $\lambda_0$ and $a_{BM}$ were determined by Anderson and Sigmund [19] by comparison with previously proposed Born-Mayer potentials. The second term $F(E)$ is the density of deposited energy at the surface and depends on the type, energy, and direction of the incident ion and the target parameters $Z_2$, $M_2$ and $n_0$. The deposited energy at the surface can be expressed as:

$$F(E) = \alpha(M_2/M_1,\ \theta)\, n_0\, S_n(E) \qquad (3.4)$$

where $n_0S_n(E) = (dE/dx)_n$ is the nuclear stopping power, the dimensionless factor $\alpha$ (the fraction of energy available for sputtering) is a function of the mass ratio between the masses of the bombarding ion ($M_1$ )and a target atom ($M_2$ ) and the angle of incidence of the surface and the ion energy [10]. Thus, equation 3.1 can be written as follows:

$$Y = 0.042\,\alpha(M_2/M_1,\ \theta)\, S_n(E)/U_0 \qquad (3.5)$$

This formula by Sigmund is used in our calculations of the sputter yields of the substrates considered in chapter 5. In the following paragraphs the individual parameters of this equation are discussed in details.

### 3.2.1 THE NUCLEAR STOPPING POWER

The derivation of the nuclear stopping was discussed in section 2.2.2. In Sigmund's equation (3.5) it can be seen that the energy dependence of the sputtering yield follows from the energy dependence of the stopping power.

Sputtering yield increases with ion energy until it reaches maximum value, then it falls off. As energy increases, the ion velocity also increases and sputtering is enhanced. Furthermore the sputtering yield increases with the increase in bombarding ion mass. The position of the maximum in the sputtering yield curve depends on the type of the bombarding ion, it moves

towards lower energies with decreasing ion mass. This is depicted in figure 3.2 below.

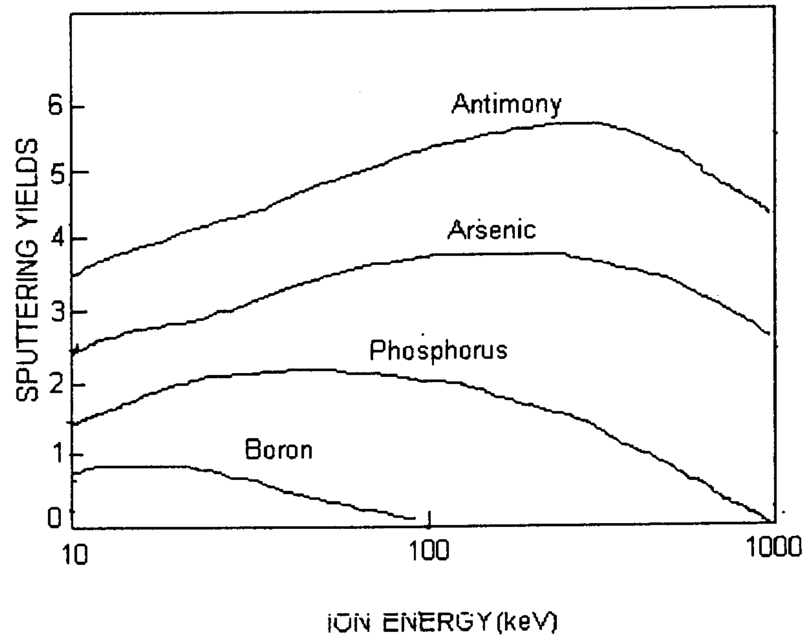


**Figure 3.2**: Sputtering yield dependence on mass and energy of an ion incident on a silicon target [20].

## 3.2.2. THE FACTOR $\alpha$

The factor $\alpha$ is the fraction of energy available for sputtering. For high energies, (i.e., $\varepsilon \geq 1$) where ε is the reduced energy parameter (see Equation 2.9), $\alpha$ depends weakly on the energy. This is due to the fact that inelastic (or electronic) stopping enhances the dwell times of the impinging ions in the near-surface region. This, in turn, influences the energy transfer. For low energies ($\varepsilon \leq 1$), $\alpha$ is, for practical purposes, independent of the energy. This is the energy regime that is important in sputtering. There are several

models for $\alpha$. The one used in our computer code for perpendicular incidence (chapter 5) is by Anderson and Bay [21].

$$\alpha(M_2/M_1) = 0.15(1+M_2/M_1)^{0.7} \tag{3.6}$$

If the bombarding ions impinge on the target with an angle of incident $\theta \leq 60°$, then $\alpha$ is given by

$$\alpha(M_2, M_1, \theta) = \alpha(M_2/M_1)cos^{-f}\,\theta \tag{3.7}$$

where

$$f = (5\pm2)/3$$

The increase in $\alpha$ in equation 3.7, with increasing $\theta$, is due to the increasing density of energy deposition near the surface plane. The yield rises at incidence angles away from the normal because there is a greater chance that the cascade is close to the surface. At the very high angles of incidence the ion beam will merely bounce off the surface so that less energy is deposited and the yield decreases. The maximum in this sputtering yield typically occurs at an angle between 50° and 80° from the normal. This equation is not valid for oblique incident ($\theta \geq 80°$) because Sigmund did not extend his theory to ion bombardment at glancing incidence. The rate of change with angle ($\theta$) is a function of $M_2/M_1$ and if $M_2 >> M_1$ the dependence is roughly $(cos\theta)^{-1}$ as was predicted by Thompson's model [22].

### 3.3.3. SURFACE BINDING ENERGY

Sigmund introduced surface binding energy by means of a barrier that must be surmounted by escaping atoms, and hence plays an important part in determining the yield of sputtered particles. An important consequence of the surface binding energy is that it has a significant influence on the directions taken by the ejected atoms. Both aspects of surface binding are important in structure-less media as well as in crystalline ones, but in the latter, there is the additional feature that the surface binding energy depends on the crystal orientation.

A correct value for the surface-binding energy term $U_0$ of the substrate in equation 3.5 is probably the most difficult problem in the Sigmund sputter theory, especially for the sputtering of compounds. For elemental and metallic substrates, surface binding energy was taken as heat of sublimation, because heat of sublimation is the energy required in dislodging atoms from the surface. This choice usually leads to reasonable agreement between theory and experiment [18]. Some authors use the related quantity, the cohesive energy (heats of atomization), since it the energy necessary to disperse a solid into its component atoms.

It is obvious that the surface-binding energy as represented by either the sublimation energy or cohesive energy is only a generalized energy for the substrate atoms. The surface-binding energy for individual surface atom may vary considerably, depending on, for example, the position of the atom, its neighbors, and the bonds between the atoms. Thus, one might expect that

even the generalized surface-binding energy of a substrate may change when a crystalline substrate changes to an amorphous state under the influence of ion bombardment. Similarly, an atom (or molecule) at a kink site will have a different binding energy than that of an atom (or molecule) in a 'flat' surface, or one at a ledge or an isolated atom (or molecule). This means that a distribution of binding energies exists for any substrates. Therefore, in equation 3.1, the surface binding energy should be a population-weighted average over the individual binding energies. For nearly all of the materials that we used, these different values do not exist. Therefore, we used the relevant heats of sublimation at 298 K as tabulated by Gschneidner [23].

# CHAPTER 4

# NUCLEAR REACTION ANALYSIS

Nuclear Reaction Analysis (NRA) method has been used for analyzing the near surface regions of a solid sample for the past 20 years. It is complementary to Rutherford Back-Scattering (RBS) method since it can detect low Z elements in a high Z host. Another important feature of NRA is the advantage of allowing a selective determination of different isotopes, being ideal for isotopic tracing experiments. The procedures used in this technique are similar to those for the RBS measurements, but the particle detected is different from the incident particle. Usually, neutrons, protons, deuterons and $\alpha$-particles are used to induce nuclear reactions on low Z nuclei. Figure 4.1 shows this situation.

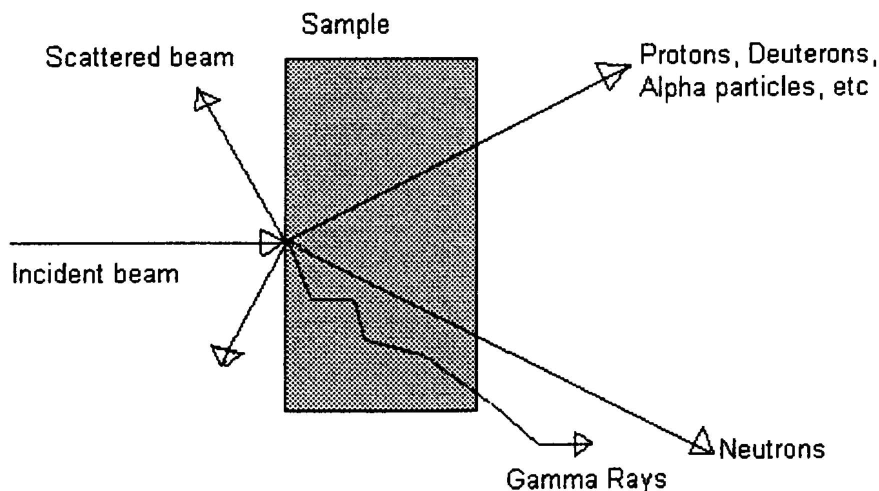


**Figure 4.1:** Schematic drawing of ion beam incident on a target with the variety of nuclear interactions that can occur.

UNIVERSITEIT VAN PRETORIA
UNIVERSITY OF PRETORIA
YUNIBESITHI YA PRETORIA

## 4.1 NUCLEAR REACTION

High-energy light ions or neutrons are penetrating deep enough into the solid to probe a relatively thick surface layer via nuclear interaction [4, 20]. Of particular interest are reactions giving rise to the emission of heavy particles such as protons or alpha particles (in contrast to light particles like electrons), since they have enough energy to travel several microns in the solid without being deflected.

A nuclear reaction is usually written in the form $A(x, y)B$, where $A$ represents the nucleus struck by a particle $x$, which leads to the formation of a new nucleus $B$ and the emission of $y$. This reaction can also be written as

$$A + x \rightarrow B + y \qquad (4.1)$$

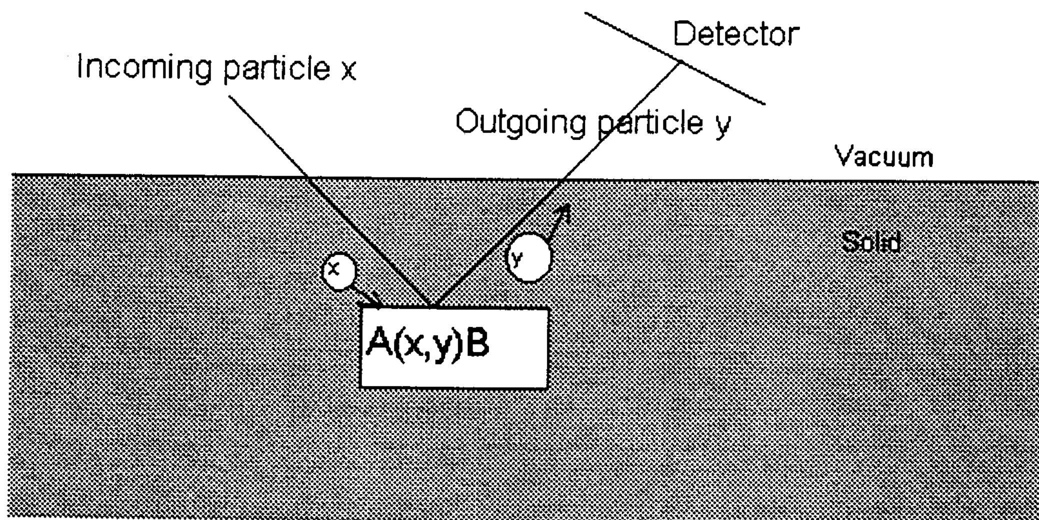


**Figure 4.2:** Nuclear reaction analysis

This situation is shown in figure 4.2. In this figure $x$ and $y$ represent the incoming and outgoing particles, respectively. The detected reaction products are usually protons, deuterons, tritons, α-particles, $^{3}$He and $\gamma$-rays. As in chemical reactions, a nuclear reaction involves an amount of energy. Since there is a transformation between the kinetic energy and the rest mass energy, then the final kinetic energy $K_B + K_y$ of the reaction products can be smaller or greater than the initial kinetic energy $K_x$ of the incident particle. The different is called the $Q$ value of the reaction:

$$Q = K_B + K_y - K_x \tag{4.2}$$

where, $K_y$ is the kinetic energy of the outgoing particle. Positive $Q$ value (exothermic reaction) results in reaction products carrying more kinetic energy than the incoming particle. As a consequence, nuclear reactions with large positive $Q$ value yield emitted particles with higher energy. This means that useful reactions for NRA are those with the larger $Q$ values. For these reactions experiment can measure a high penetration depth and also, if the energy is well above that of the incident particles, a background free detection is achieved, because the elastically scattered incident ions can be separated from the reaction yield.

Alternatively, the reaction energy can be negative so that the reaction only takes place when the energy of incident radiation exceeds the threshold energy. As the charged particle penetrates the sample it undergoes energy loss through inelastic collisions and this can be used to derive information on the depth distribution of a particular nuclide.

The profile of implanted impurities can be measured by non-resonant and resonant nuclear reactions. The difference between the two classes of reactions is based on the shape of the differential cross section as a function of the energy, which dictates how the experiment can be done. The disadvantage of the non-resonant reaction is the poor depth resolution for thick targets. The resonant reaction is discussed below.

## 4.2 RESONANCE REACTION

Many nuclear reactions have one or more sharp resonances as a function of incident particle energy. The use of the resonance method in the depth profiling of impurity takes advantage of the sharp peak in the nuclear reaction cross section. When the energy of the incident projectile approaches the resonance energy $E_R$, the greatly increased cross section produces a larger yield of the out coming particles or $\gamma$-rays. In this way, the width of the resonance peak determines the depth resolution for this particular reaction. The procedure for the resonant NRA is shown below in figure 4.3, where the out coming reaction products are $\gamma$-rays. We assume that a target of mass $M_2$ is implanted with an impurity of mass $M_1$ and analyzed by resonant nuclear reactions detecting $\gamma$-rays [4]. The distance $x$ and the depth resolution at the surface (see figure 4.3), defined as the full width at half maximum of the measured profile is obtained using the expressions 4.3. The depth $x$ and the projectile energy $E_p$ are related through the equation

$$E_p = E_R + (x/\cos\theta)(dE/dx) \qquad (4.3)$$

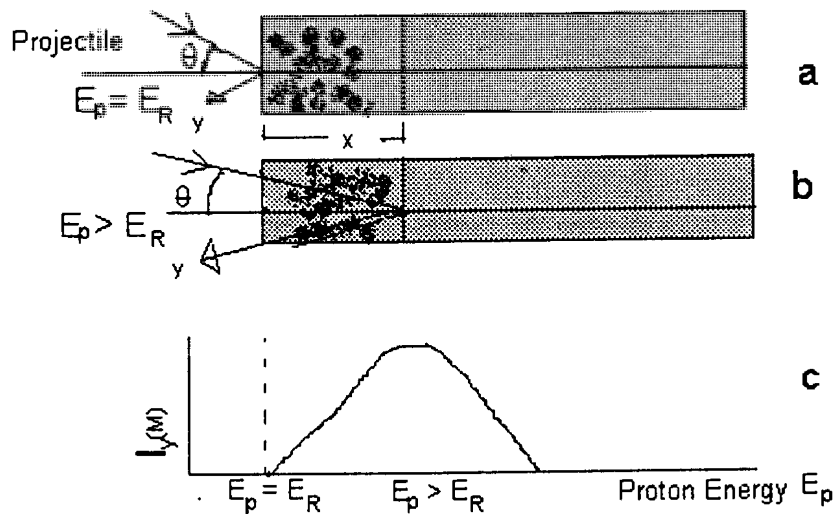


**Figure 4.3:** NRA for a resonant cross section. A target of mass $M_2$ with impurities of mass $M_1$ is analyzed by resonant nuclear reactions detection $\gamma$-rays. (a) and (b) show respectively the reactions for projectile energy $E_p = E_R$ and $E_p > E_R$. (c) is the excitation function for the corresponding yields $I_\gamma(M_1)$ of the impurity atoms.

Here $\theta$ is the angle between the incident particle and the surface normal. For the conversion of the measured energy yield to depth penetration, it is necessary to know the stopping cross section of the incident ions in the target material and the resonance energy for the specific nuclear reaction. The stopping power ($dE/dx$) for the incident beam is assumed to be constant, because of the surface approximation, where $x$ is assumed to be small. The depth resolution is determined by the width of the reaction and the fluctuation in energy $\delta E_p$ of the bombarding ions given by equation 2.25 and 2.26.

There exists a great number of resonance reactions of the (p, $\gamma$) type. A good example is the $^{27}$Al(p, $\gamma$)$^{28}$Si reaction occurring at a proton energy of 992

keV, and showing a full width at half maximum of only 0.1 keV. The decay scheme of the 12.542 MeV excited level in $^{28}Si$ together with spin and parity assignment of some of the energy levels is represented in figure 4.4. The 12.542 MeV excited level in $^{28}Si$ decays with probability of 78%[24-26] to the 1.78 MeV excited state. Other important decay channels of this level are leading to the 7.8 MeV level with a probability of 12% and to the 7.93 MeV excited level with a probability of 5%. In the experiments by Hayes [27] the energy window between 9.5 and 11.0 MeV is used to detect the full energy peak and its escape peaks.

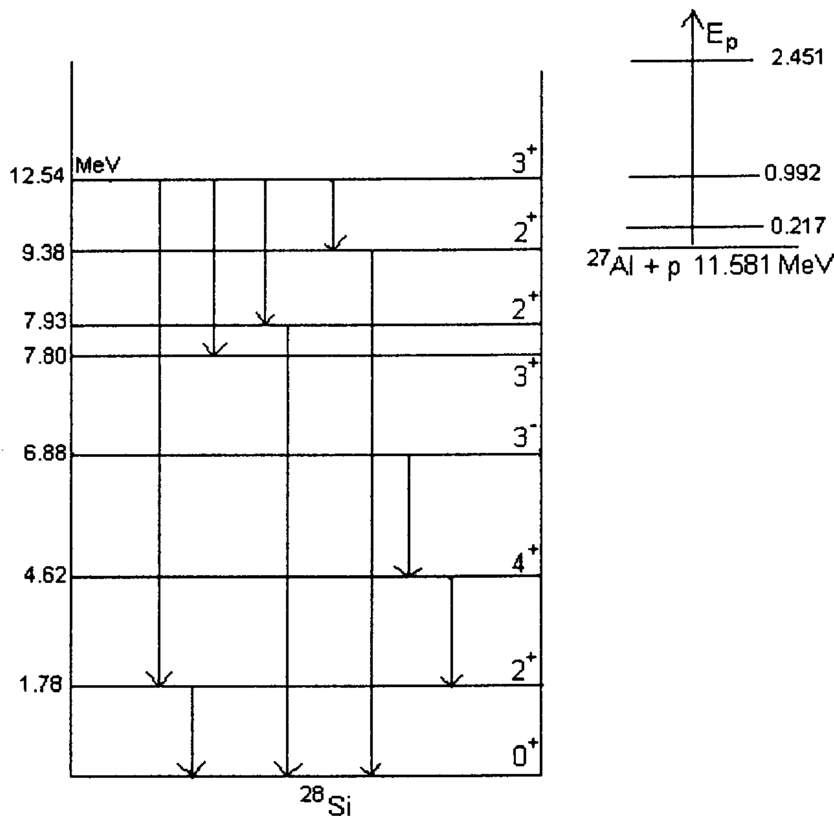


**Figure 4.4:** The decay scheme of some the $^{28}Si$ transition from the 12.542 MeV excited level

# CHAPTER 5

# METHOD OF SPUTTERING CORRECTION OF IMPLANTED IONS IN METALS

Sputtering plays an important role in the modification of implanted profiles. In this study we have investigated the effect of target sputtering on the experimentally observed depth profiles for aluminium ions implanted at 150 keV into a number of metals with the atomic number in the range of $23 \leq Z_2 \leq 78$. Sputtering effects are studied in this project as a function of sputtering coefficients and fluence. This is achieved by employing theoretical predicted profiles to observe how they are affected by sputtering effects

## 5.1 THE ASSUMPTIONS OF THE METHOD

The assumptions made in this study are described briefly here. As a first order approximation, the theoretical depth profiles predicted by TRIM code were used in this study in order to study the effects caused by sputtering on the implantation depth profile. TRIM was used in this study because it is easily available and is reasonably well describing the experimental depth profiles. TRIM has been used to compare with experimental results in many publications [3,6,28-30]. General agreement has been observed between the experimental results and TRIM predictions. Any distribution function that gives a realistic depth distribution profile could have been used to study sputtering effects on implanted profiles. TRIM like any simulation program

available so far, does not account for sputtering effects on the final depth distribution [31]. It was assumed that the target composition remains constant throughout the implantation. Processes like diffusion were not taken into account.

## 5.2 DESCRIPTION OF THE ALGORITHM

The method used in this study follows a numerical approach to simulate the sputtering effects on the depth profile. The implantation process is modelled by a computer code as follows: the total dose is divided into a large number (N~100) of small and equal fractional doses, i.e. $\Delta\phi = \phi/N$. For dose $\Delta\phi$ the fractional concentration profile is obtained from TRIM. The layer sputtered off the target during implantation is calculated for $\Delta\phi$ by assuming a relevant sputtering coefficient and is truncated at the origin to show that erosion occurs on the surface. Then the next implantation of $\Delta\phi$ is done to form an accumulated depth profile. Again the layer sputtered off the target surface is removed from the accumulated depth profile. This procedure is repeated with all the other fractional doses and the final depth profile is obtained. This procedure is shown by a flow chart in figure 5.1.

## 5.3 CALCULATIONS

The computer program was written to calculate sputtering yields for ion and target materials for a given energy, using Sigmund's theory for linear cascade sputtering and assuming surface binding energies equal to the relevant heats of sublimation at 298 K as tabulated by Gschneidner [20].

Sputtering coefficients range between approximately 1.4 and 4.0 atoms/ion. The estimated layer thickness sputtered off from the samples by a dose of 5 $\times$ $10^{16}$ $Al^+$ $cm^{-2}$ at 150 keV varied between about 10 nm and 50 nm. For the relatively small sputtering depths encountered in this work, the only significant change observed is a reduction of the projected range, while the influence on the higher range moments is in most cases negligible.

## 5.4 SPUTTERING CORRECTION FACTORS

The sputtering correction factors $F_i$ (for, $i$ =1,2) were calculated by dividing the range moments for the uncorrected TRIM profile by the range moments for the corrected TRIM profile as follows:

$$F_1 = R_{p(\text{TRIM without sputter correction})} / R_{p(\text{TRIM with sputter correction})}$$

and

$$F_2 = \Delta R_{p(\text{TRIM without sputter correction})} / \Delta R_{p(\text{TRIM with sputter correction})}$$

We then correct the first two experimental range moments by multiplying them with these sputtering correction factors $F_i$. The corrected results for the projected range $R_p$ and the standard deviation $\Delta R_p$ of the investigated nine metals are given in table 6.1. Together with the sputtering correction factors and are compared with the corresponding TRIM predictions.

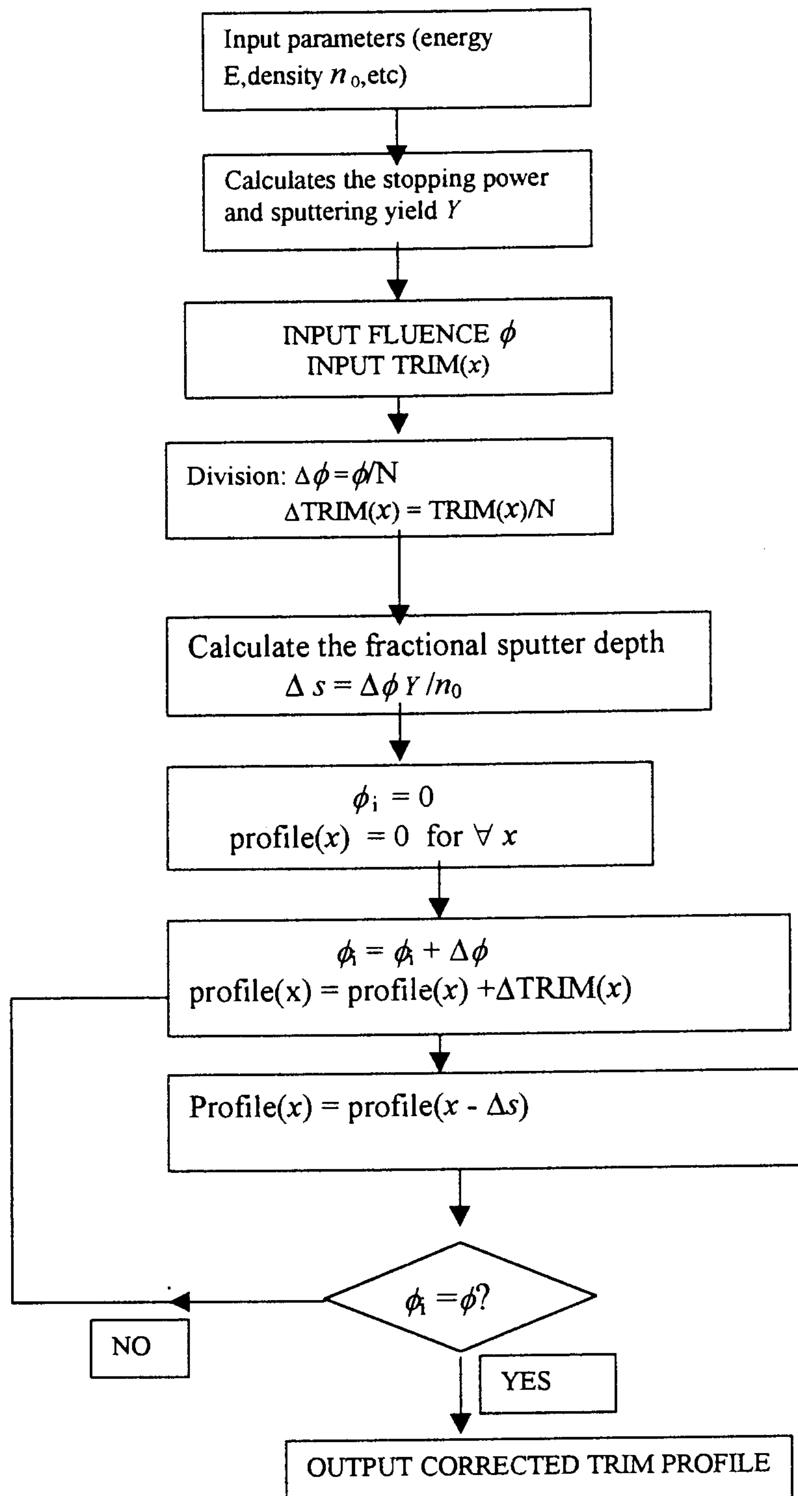


**Figure 5.1 Flow chart of the sputtering correction algorithm.**

# 5.5 TESTING OF THE METHOD

To test the validity of this method, correction factors were calculated for a gaussian distribution function instead of TRIM. This was done to compare the numerical result with results of an analytic method described below, which can calculate the sputtering effects only for a gaussian profile [32].

## 5.5.1 GAUSSIAN APPROXIMATION

The modification of the implantation profile due to sputtering can be calculated analytically, if the sputtering yield and the target atomic density remain constant and the implanted ions have a gaussian depth distribution [33]. The normalized gaussian distribution function is defined as follows:

$$p(x') = (1/(2\pi)^{1/2}\Delta R_P)\exp[-(x'-R_P)^2/2\Delta R_P{}^2] \qquad (5.1)$$

An increase in impurity density $dn(x', \varphi)$ is related to the range distribution $p(x', \varphi)$ by,

$$dn(x', \varphi) = \mathrm{p}(x', \varphi)\, d\varphi \qquad (5.2)$$

Therefore

$$dn(x',\varphi) = (1/(2\pi)^{1/2}\Delta R_P)\exp[-(x'-R_P)^2/2\Delta R_P{}^2]d\varphi \qquad (5.3)$$

When the surface is eroded due to sputtering, the origin of the x` coordinate system changes its position continuously with the dose during implantation. The layer sputtered off the surface during implantation is given by,

$$dx`(\varphi)=d\varphi Y/n_0 \tag{5.4}$$

where $Y$ is the sputtering yield. Now, if sputtering is considered then the accumulated impurity distribution $n(x`,\Phi)$ is obtained by integrating for all $\varphi \leq \Phi$,

$$n(x`,\Phi)=(1/(2\pi)^{1/2}\Delta Rp)\int_0^{\Phi}\exp[-(x`-x`(\varphi)-R_p)^2)/2\Delta Rp^2]d\varphi \tag{5.5}$$

where $\Phi$ is the total bombarding fluence. The final position of the surface, $x`(\Phi)$, after complete bombardment is

$$x`(\Phi)=s=1/n_0\int_0^{\Phi}Yd\varphi \tag{5.6}$$

$x`(\Phi)$ is equal to the total thickness sputtered, $s$. Now defining a new coordinate $x$ with its origin at the final surface,

$$x=x`-s$$

then,

$$n(x,\Phi)=(1/(2\pi)^{1/2}\Delta Rp)\int_0^{\Phi}\exp[-(x+s-x`(\varphi)-R_p)^2)/2\Delta Rp^2]d\varphi \qquad (5.7)$$

Let $z = s - x`(\varphi)$, then it follows from equation 5.4 that

$$dz = -dx`(\varphi) = -(n_0/Y)d\varphi$$

The integration limit at final surface will be as follows:

If $x`(\varphi) = 0$, then $z = s$

If $x`(\varphi) = s$, then $z = 0$

Therefore, the concentration defined by $c\ (x,\ \Phi) = n(x,\ \Phi)/n_o$ is given by

$$c(x,\Phi)=(1/(2\pi)^{1/2}\Delta RpY)\int_0^{s(\Phi)}\exp[-(x+y-R_p)^2)/2\Delta R_p^2]dz \qquad (5.8)$$

Thus, the solution of this equation is expressed in terms of error function,

$$c(x,\Phi) = (1/2Y)[erf\{(x - Rp + s(\Phi))/\sqrt{2}\Delta Rp\} - erf\{(x - Rp)/\sqrt{2}\Delta Rp\}] \qquad (5.9)$$

## 5.5.2. COMPARISON OF THE NUMERICAL AND THE ANALYTIC METHODS.

A gauss distribution with the typical parameters of vanadium was used in comparing the numerical method with the analytical method. The parameters

are as follows: $R_p$ = 130 nm, $\Delta R_p$ = 49 nm, $Y$ = 1.43 at/ion, $U_0$ = 2.33 eV/at and $\Phi$ = $5 \times 10^{16}$ ions/cm$^2$ (500 ions/nm$^2$). The gaussian distribution profile defined by equation 5.1 is used as an input profile in the sputtering correction computer program instead of using a TRIM profile. A modified depth distribution in which sputtering has been corrected is obtained. Comparing that depth distribution with the distribution found analytically from equation 5.9, a good correlation is found.

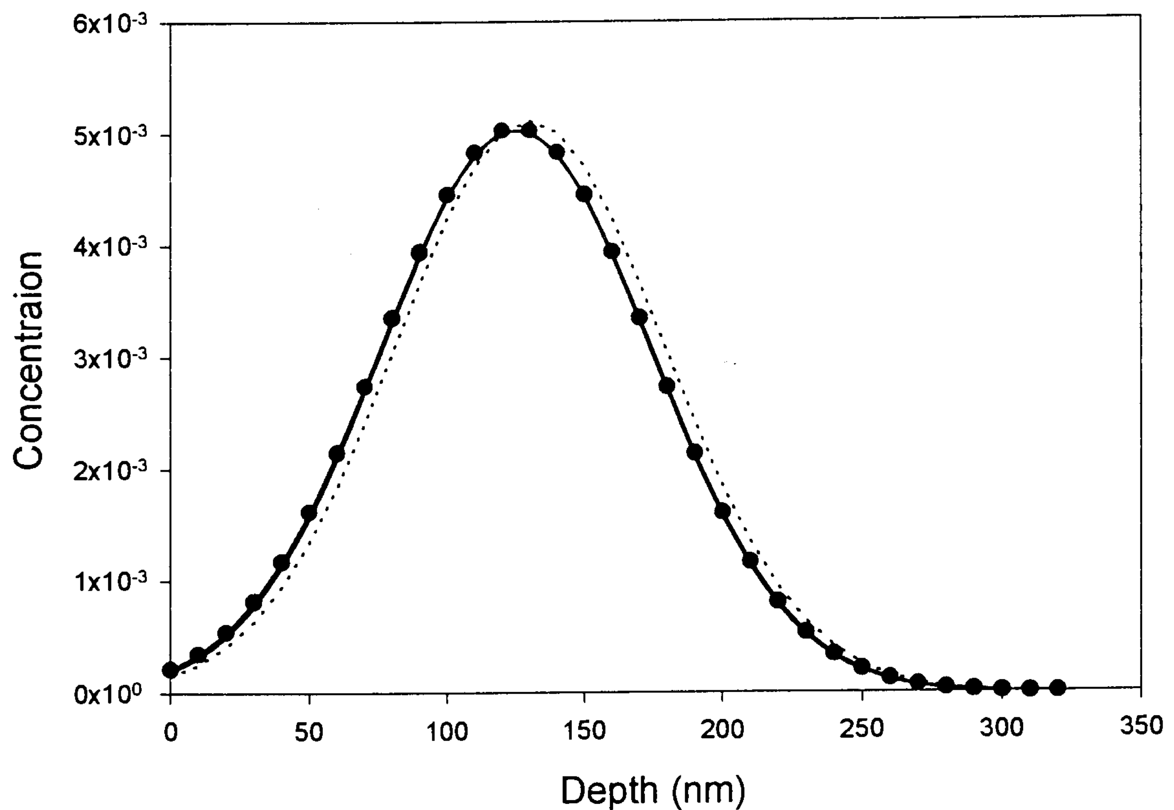


**Figure 5.2**: Concentration profile calculated numerically from a gaussian concentration function c(x) plotted as points and the one calculated from equation 5.9 plotted as a solid line are compared with uncorrected gaussian profile plotted with dashes.

The correction factors for the profile found by using the numerical method are as follows: $F_1$ = 1.036 and $F_2$ = 1.00, which are similar to the ones we found for the analytical method ($F_1$ =1.038 and $F_2$ =0.99). The two distributions are plotted in figure 5.2 above. It is evident from figure 5.2 that the sputtering correction method we developed agrees with the analytic method. This justifies the adoption of this method for the cases studied in this project, which should be generally valid.

## 5.6 APPLICATION OF THE SPUTTERING CORRECTION METHOD

In this section the method is used to study the effect of $Y$ and $\Phi$ on the depth profiles. The variation of the implantation depth profile as a function of implanted dose and sputtering yield is studied by using two hypothetical cases, firstly if the dose is kept constant and the sputtering yield is varied and vice versa.

### 5.6.1 DEPTH PROFILES AS A FUNCTION OF THE SPUTTERING YIELD

The change of the implantation depth profiles for $\Phi$ = 5x10$^{16}$ Al$^{+}$cm$^{-2}$with sputtering yield is depicted in the figures 5.3 and 5.4 for the hypothetical cases with typical parameters of vanadium and platinum respectively. For sputtering yield of $Y$=1 at/ion most of the ions in the incident beam are

retained, hence the effect of sputtering is negligible. As sputtering yield increases the sputtered depth also increases and the depth profile maximum starts to reduce and shifts towards the surface. Hence the depth profile maximum in the hypothetical case with typical parameters of vanadium for the $Y$=1, 7, 12 at/ions in figure 5.3, is approximately at the positions 1310, 1140, and 1020 angstroms respectively.

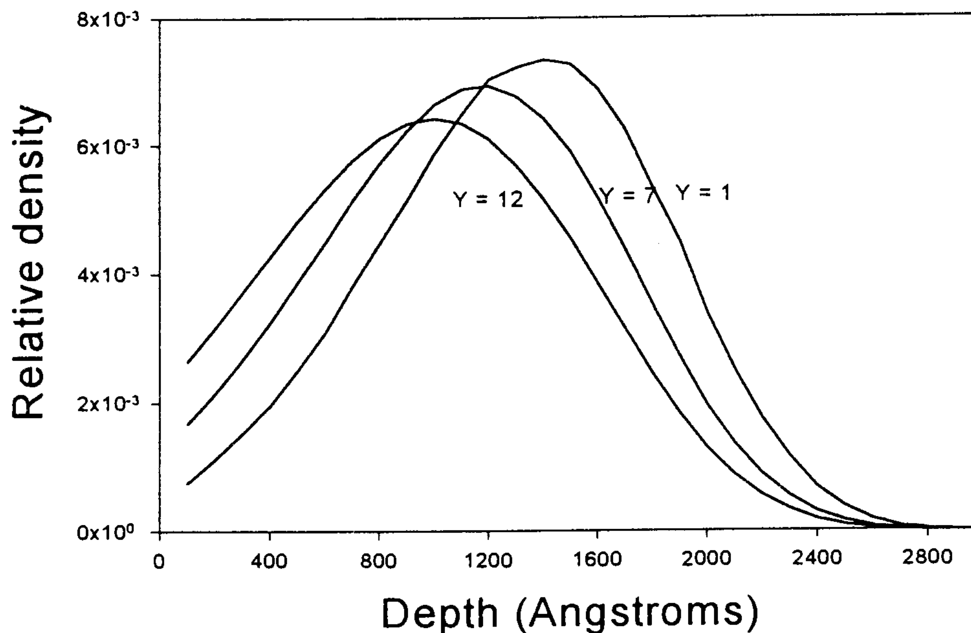


**Figure 5.3**: Aluminium implantation profiles for different sputtering yields of a hypothetical material with the typical parameters of vanadium at a fixed fluence of $5 \times 10^{16}/cm^2$

While for the hypothetical case with the typical parameters of platinum, the profile maximum for $Y$=1, 7, 12 ions/atom in figure 5.4 is approximately at the position 740, 620 and 570 angstroms respectively. Low atomic number

targets are less affected by sputtering compared to high atomic number targets. For instance from figures 5.3 and 5.4 it is obvious that less sputtering effects occur in the case of vanadium, while for platinum there is a significant change of the depth profile.

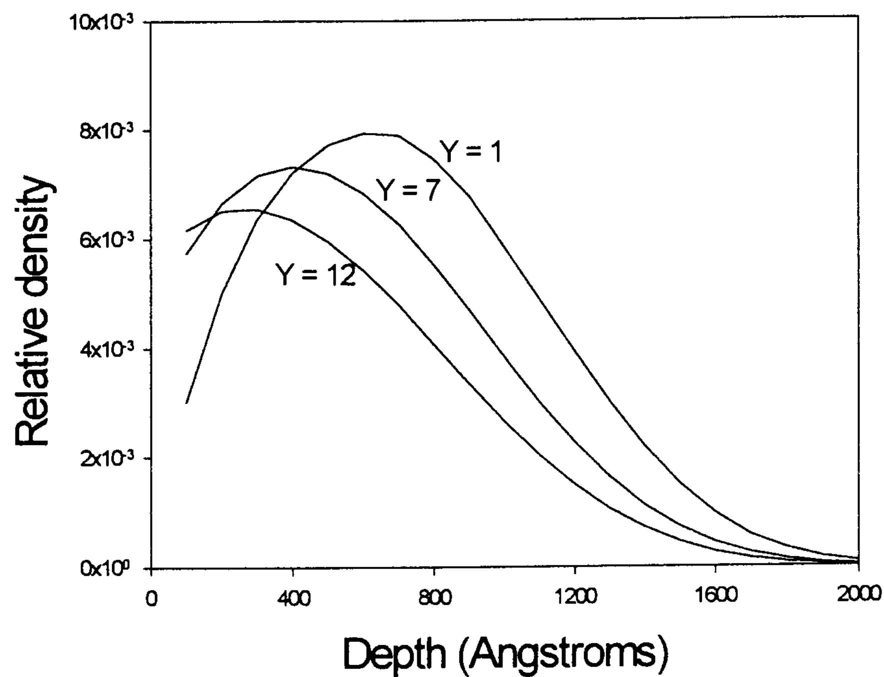


**Figure 5.4**: Aluminium implantation profiles for different sputtering yields of a hypothetical material with the typical parameters of platinum at a fixed fluence of $5x10^{16}$ $Al^{+}/cm^{2}$.

### 5.6.2 DEPTH PROFILES AS A FUNCTION OF THE FLUENCE

The change of the shape of the depth profile as a function of the fluence (dose) is shown in figures 5.5 and 5.6 for vanadium with $Y = 1.43$ and platinum with $Y = 4.0$ respectively. For low doses between $5\text{x}10^{13}$ - $5\text{x}10^{15}$ ions/cm$^2$, little sputtering occurs and can be safely neglected. The depth profiles of these doses lie on top of each other when plotted on the same axis, for this reason the latter two were omitted in figures 5.5 and 5.6. Profile changes starting from a dose of $5\text{x}10^{16}$ cm$^{-2}$ are noticeable as already discussed by [34-36]. As fluence increases, the surface erosion increases and the profile maximum concentration starts to shift toward the surface.

For higher doses $\Phi > 5\text{x}10^{16}$ ions/cm$^2$ the peak of the implanted profile shifts rapidly towards the surface. Again there is a significant change on the depth profile in the case of platinum compared to vanadium, because low atomic number targets often have lower atomic density and sputtering yields than high atomic number targets. For instance, for the dose of $5\text{x}10^{17}$ the peak of the depth profile in the case of platinum has already reached the surface, while in the case of vanadium it is far from reaching the surface.

For very high fluences above $5 \times 10^{18}$ peak maximum reaches the surface and this sputtering correction method still gets correct depth distribution, but the correction factors becomes meaningless as the shape changes drastically. For these doses saturation is reached.

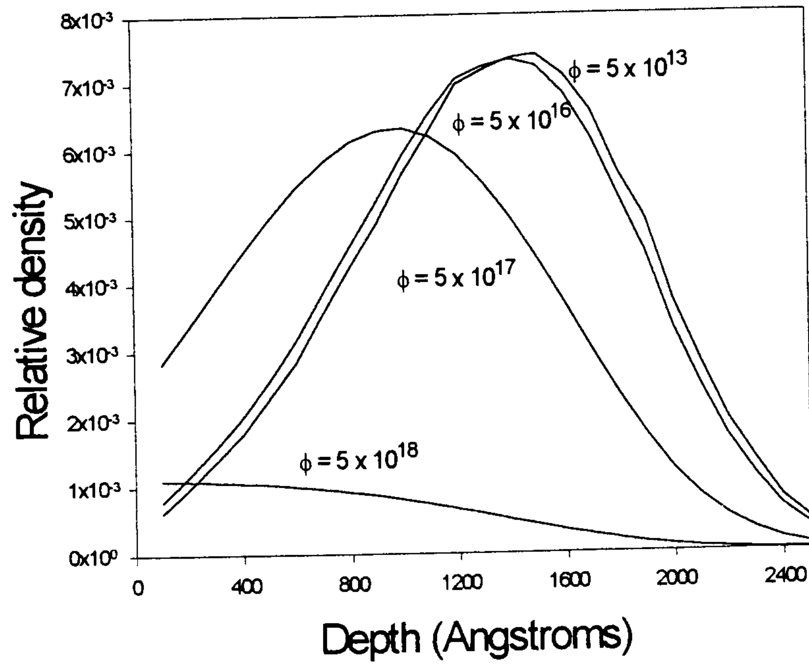


**Figure 5.5:** Aluminium implantation profiles for different fluences of vanadium implanted at a fixed sputtering yield of 1.43.

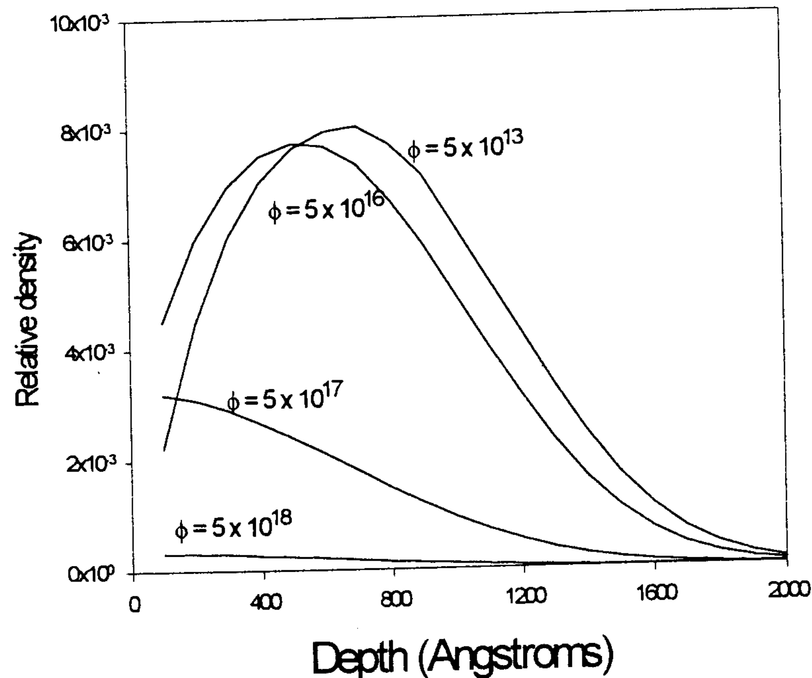


**Figure 5.6:** Aluminium implantation profiles for different fluences of platinum implanted at a fixed sputtering yield of 4.0 ions/cm$^2$.

## 5.7 RETAINED FLUENCE

The number of implanted atoms that remain in the sample after implantation is referred as retained dose (fluence). This retained dose is always less than the incident dose as there is a finite probability of both ion reflection and target sputtering occurring. With increasing incident dose, the discrepancy

becomes larger as the concentration approaches saturation. A small and approximately constant proportion of the incident ions will generally be lost due to ion reflection. Reflection loses are greatest for low energy light ions incident upon a heavy substrate. The loss is smallest for high-energy implants, because they penetrate deep into the target.

The loss caused by sputtering will be highly dependent upon the dose. For low doses, say less than $10^{14}$ ions/cm$^2$, the loss is small. For doses of $10^{16}$-$10^{17}$ ions/cm$^2$ the loss may be detectable and for higher doses the concentration will approach saturation. The losses by reflection and sputtering are additive and together are cause of the difference between the incident dose (fluence) and the retained dose [37]. The percentage retained dose for all target materials used in this study is shown table 6.2.

# CHAPTER 6

# ANALYSIS OF EXPERIMENTAL PROFILES

The experimental depth distributions obtained by Hayes [28] of aluminium implanted at 150 keV into the polycrystalline sample of vanadium, chromium, manganese, cobalt, yttrium, hafnium, tantalum and platinum at room temperature are analysed in this chapter. Relatively high doses ($\Phi \geq 5 \times 10^{16}$) were implanted to ensure satisfactory counting statistics and target sputtering effects become important, especially for heavier target materials ($Z_2 \geq 50$).

## 6.1 ALUMINIUM IMPLANTED INTO VARIOUS METALIC TARGETS

Summary of results for aluminium implanted into different polycrystalline metallic targets are shown in figure 6.1 to figure 6.9. The theoretical predictions of TRIM before and after sputtering correction are compared with the experimental depth profiles. The experimental errors presented in table 6.1 for the first two range moments are due to the uncertainty in proton stopping powers and the statistical counting fluctuations as calculated by Hayes [27]. In the case of the projected range the experimental uncertainty of the position of the surface is also taken into account. For these estimates it was assumed that the stopping powers are accurate within 5%, while the statistical contribution to the experimental error was obtained by a fitting

procedure, which describes the experimental depth profile by a distribution function in terms of the first four range moments. These four range moments are the projected range, range straggling, skewness and kurtosis.

**Table 6.1:** First two experimentally determined range moments of 150 keV $Al^+$ ions implanted into targets at room temperature after sputtering correction. Also given are the calculated sputtering yields Y and the correction factors $F_i$ used for correcting $R_p$ and $\Delta R_p$

| Target | Y | PROJECTED RANGE | | | STRAGGLING | | |
|---|---|---|---|---|---|---|---|
| | Atoms/ion | $R_p$ (nm) | $F_1$ | $R_{EXP}/R_{TRIM}$ | $\Delta R_p$ (nm) | $F_2$ | $\Delta R_{EXP}/\Delta R_{TRIM}$ |
| V | 1.43 | 132±8 | 1.02 | 1.01±0.06 | 50±4 | 1.00 | 0.98±0.08 |
| Cr | 1.95 | 120±7 | 1.03 | 1.04±0.06 | 49±3 | 1.00 | 1.09±0.09 |
| Mn | 2.85 | 102±6 | 1.04 | 0.87±0.05 | 40±3 | 1.00 | 0.82±0.06 |
| Co | 2.03 | 95±6 | 1.03 | 0.97±0.06 | 40±3 | 1.00 | 1.01±0.08 |
| Y | 3.01 | 204±13 | 1.10 | 0.98±0.06 | 85±7 | 1.00 | 0.93±0.08 |
| Hf | 3.44 | 121±8 | 1.12 | 1.14±0.08 | 63±3 | 1.02 | 1.16±0.09 |
| Ta | 2.71 | 72±4 | 1.09 | 0.82±0.05 | 38±3 | 1.02 | 0.82±0.06 |
| W | 2.56 | 87±7 | 1.07 | 1.11±0.09 | 38±3 | 1.01 | 0.92±0.07 |
| Pt | 3.96 | 75±5 | 1.12 | 1.04±0.07 | 39±3 | 1.03 | 0.99±0.08 |

Furthermore, the uncertainty of the surface was taken as the depth equivalent of half the channel width of the experimental excitation curve. Table 6.2 shows the retained dose due to ion sputtering and reflection.

**Table 6.2:** The retained dose due to sputtering and reflection.

| Target | Retained dose | Target | Retained dose | Target | Retained dose |
|---|---|---|---|---|---|
| V | 99.7% | Co | 99.3% | Ta | 96.7% |
| Cr | 99.5% | Y | 98.1% | W | 96.8% |
| Mn | 99.1% | Hf | 95.3% | Pt | 94.0% |

### 6.1.1 ALUMINIUM IMPLANTED INTO VANADIUM

The depth distribution of aluminium ions implanted into vanadium is depicted in figure 6.1. It is clear from the figure that the experimental profile is in good agreement with the corrected theoretical TRIM-95 profiles.

Al implanted into V at 150 keV

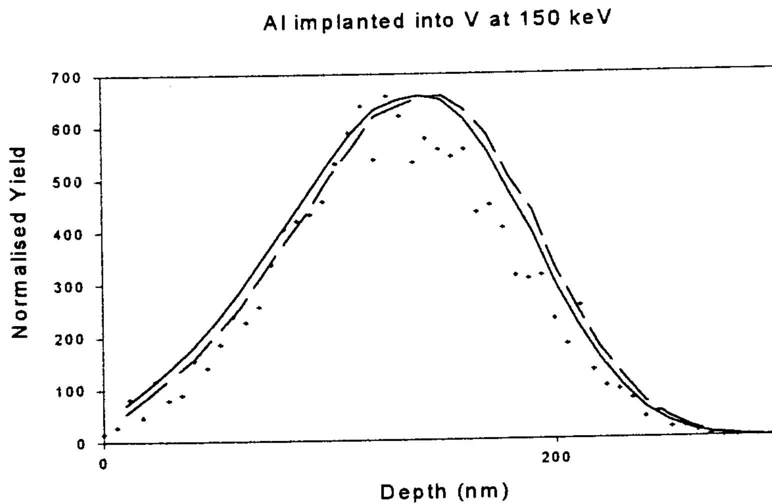


**Figure 6.1:** Experimental aluminium profiles(symbols) in vanadium for an implantation dose of 5 x $10^{16}$ $Al^{+}$ $cm^{-2}$ at 150 keV compared with TRIM-95 before(dashes) and after(solid line) taking sputtering into account.

Relatively small sputtered layer of 10 nm was found for vanadium, for a calculated sputtering coefficient of 1,43 atoms/ion. The influence of sputtering on the experimentally determined first range parameter is found to be less than 2%, while the effect on the higher range parameters is so small that it can safely be neglected. Furthermore 99% of the implanted ions are retained in the sample.

### 6.1.2 ALUMINIUM IMPLANTED INTO CHROMIUM

Figure 6.2 shows the depth distributions of aluminium ions implanted into chromium. It is evident from the figure that there is excellent agreement

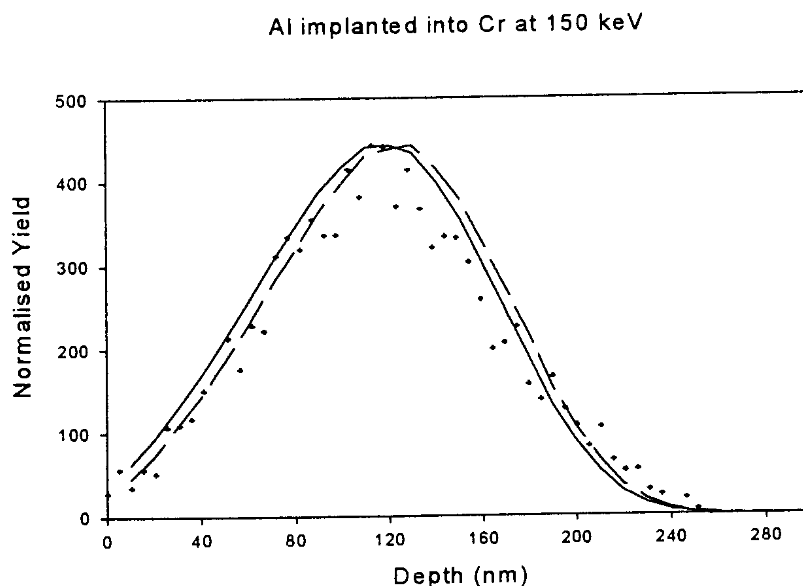


**Figure 6.2:** Experimental aluminium profiles(symbols) in chromium for an implantation dose of 5 x $10^{16}$ $Al^{+}$ $cm^{-2}$ at 150 keV compared with TRIM-95 before(dashes) and after(solid line) taking sputtering into account.

between the experimental profile and the corrected theoretical TRIM-95 profile. Relatively small sputtered layer of about 10.5 nm is found for chromium, for a sputtering coefficient of 1.75 atoms/ion. The experimentally determined first range moment was found to be 4% less than the theoretical predicted projected range, which is still within the experimental error. No significant deviation is found for the second moment after sputtering correction. Furthermore 99% of the implanted ions are retained in the sample.

### 6.1.3 ALUMINIUM IMPLANTED INTO COBALT

The depth profile of aluminium ions implanted into Cobalt is shown in figure 6.3. It can be seen that the experimental profile agrees well with the

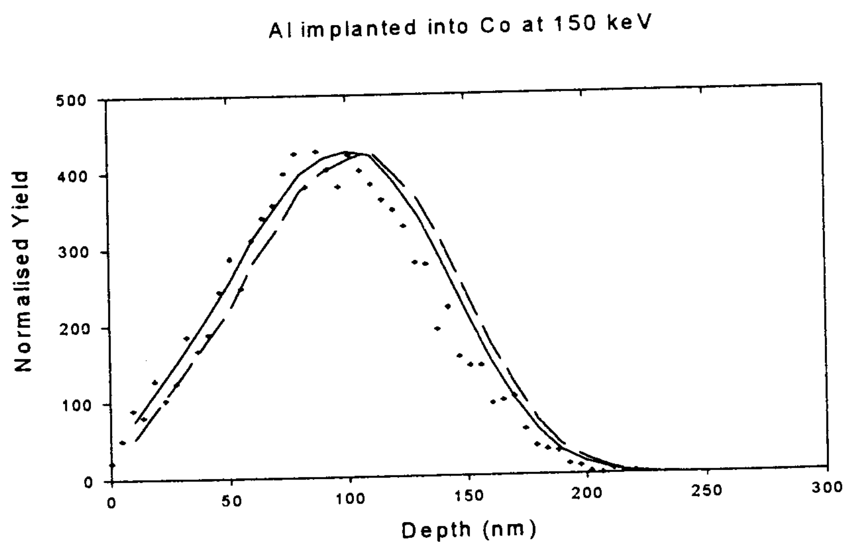


**Figure 6.3:** Experimental aluminium profiles(symbols) in cobalt for an implantation dose of 5 x $10^{16}$ $Al^+$ $cm^{-2}$ at 150 keV compared with TRIM-95 before(dashes) and after(solid line) taking sputtering into account.

theoretical profile. Again relatively small sputtered layer of about 10.2 nm was found for a sputtering coefficient of 1.83. The experimentally determined first range moment was found to be 3 % less than the theoretical predictions and second range moment by 0.2% which is very small and can be safely neglected.

### 6.1.4 ALUMINIUM IMPLANTED INTO YTTRIUM

Figure 6.4 shows the results of aluminium implanted into yttrium. Fair agreement is seen between the experimental results and the theoretical predictions. Large sputtered layer of about 50 nm is calculated for a sputtering coefficient of 2.68. Comparing the two theoretical profiles one

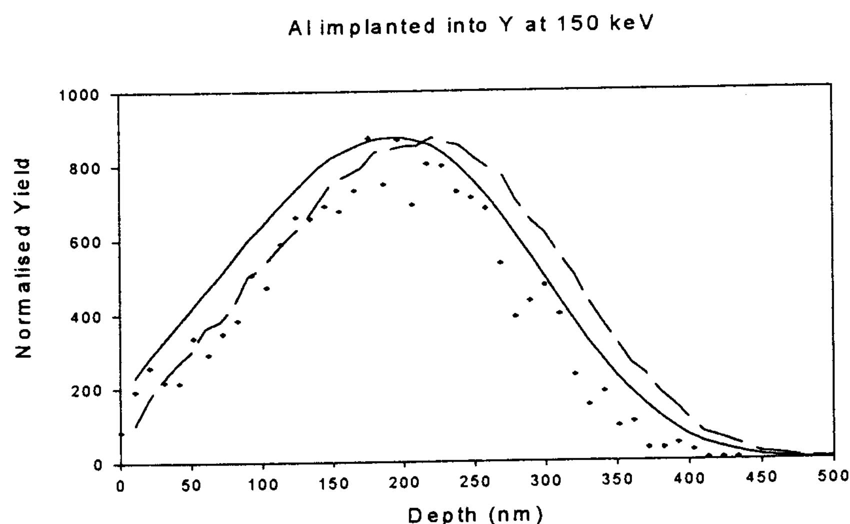


**Figure 6.4:** Experimental aluminium profiles(symbols) in yttrium for an implantation dose of 5 x $10^{16}$ $Al^+$ $cm^{-2}$ at 150 keV compared with TRIM-95 before(dashes) and after(solid line) taking sputtering into account.

before sputtering corrections and the one after sputtering corrections, one can clearly see that there is a peak shift towards the surface that shows the effect of sputtering. The experimental projected range was found to be 2% less than the theoretical prediction, but still falls within the experimental error. Fair agreement is seen between the experimentally determined second range moment and theoretical TRIM-95 estimate.

### 6.1.5 ALUMINIUM IMPLANTED INTO PLATINUM

The depth profiles of aluminium implanted into platinum is depicted in figure 6.5, which has a large sputtering coefficient of about 4 resulting in a sputtered layer of 26.1 nm. There is a good agreement between the

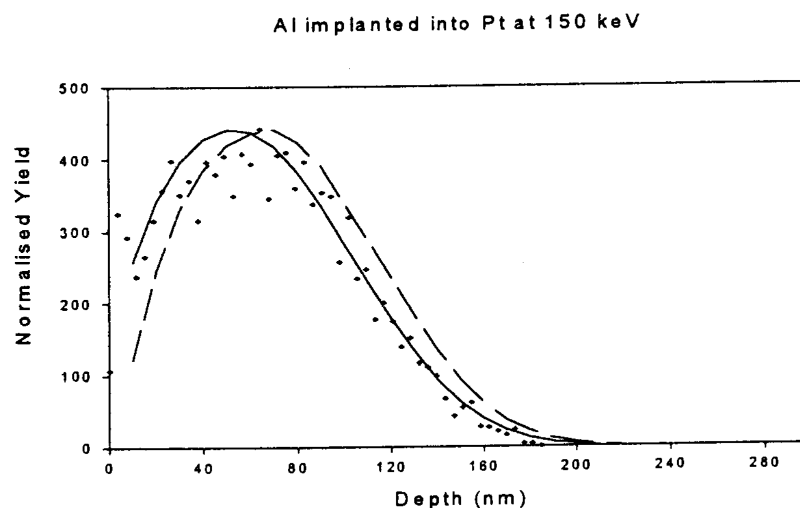


**Figure 6.5:** Experimental aluminium profiles(symbols) in platinum for an implantation dose of 5 x $10^{16}$ $Al^+$ $cm^{-2}$ at 150 keV compared with TRIM-95 before(dashes) and after(solid line) taking sputtering into account.

sputtered layer of 26.1 nm. There is a good agreement between the experimental and the theoretical depth profiles. Due to sputtering the experimentally determined first range moment was reduced by more than 12% together with a 3% change of the second range moment. Only 94% of the implanted aluminium impurity atoms are retained in the platinum sample. Furthermore, as about 14% of the ions are backscattered from the surface, the effective implantation dose in platinum is reduced to approximately $4\times10^{16}$ $cm^{-2}$.

### 6.1.6 ALUMINIUM IMPLANTED INTO MANGANESE

Figure 6.6 depicts the results for implantation of aluminium into manganese sample. It is evident from the figure that there is serious disagreement

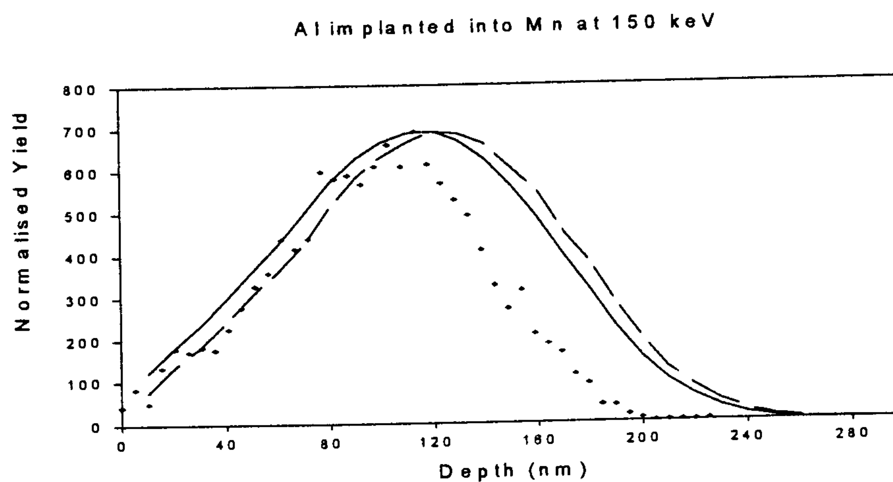


**Figure 6.6:** Experimental aluminium profiles(symbols) in manganese for an implantation dose of 5 x $10^{16}$ $Al^{+}$ $cm^{-2}$ at 150 keV compared with TRIM-95 before(dashes) and after(solid line) taking sputtering into account.

between the theoretical TRIM-95 profiles and the experimental one. A sputtered layer of 19 nm was calculated for a sputtering coefficient of 2.85. The experimentally determined first range moment was to be less by 13% when compared to the TRIM-95 value and is found to be outside the experimental error. Also the experimentally determined second range moment was found to be 18% smaller than the theoretical prediction, which is also outside the experimental error of 6%.

### 6.1.7 ALUMINIUM IMPLANTED INTO TANTALUM

Tantalum implanted with aluminium is shown in figure 6.7. It can be seen from the figure there is a serious disagreement between the experimental and

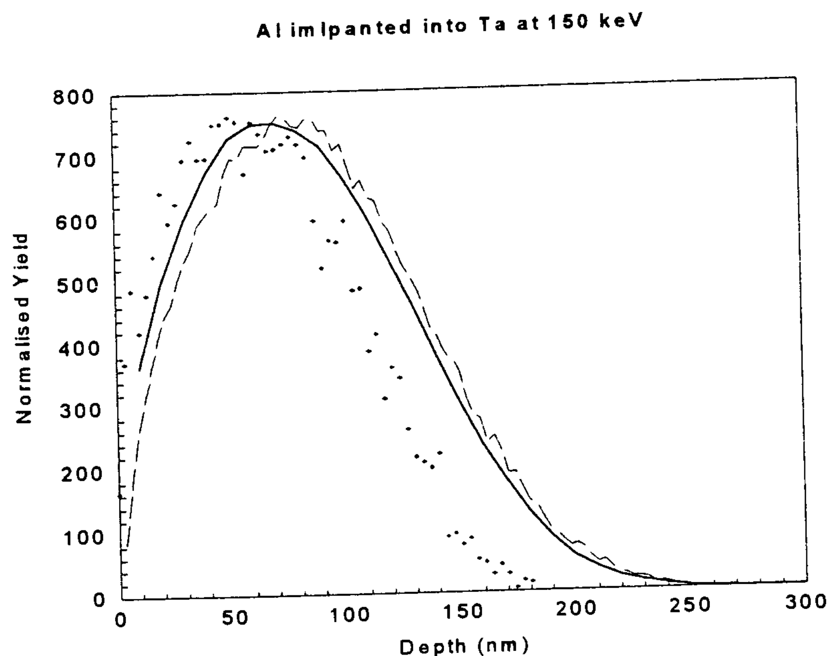


**Figure 6.7:** Experimental aluminium profiles(symbols) in tantalum for an implantation dose of 5 x $10^{16}$ $Al^+$ $cm^{-2}$ at 150 keV compared with TRIM-95 before(dashes) and after(solid) taking sputtering into account.

theoretical profile. A sputtered depth of 17 nm was calculated for a sputtering coefficient of 2.38 atoms/ion. The experimentally determined projected range was found to be lower by 18% than the values predicted by TRIM-95. This discrepancy cannot be explained by the experimental error. Again there is serious disagreement between the second experimental and theoretical range moments and the discrepancy is also outside the experimental error.

### 6.1.8 ALUMINIUM IMPLANTED INTO TUNGSTEN

The depth profile of tungsten sample implanted with aluminium is depicted in figure 6.8. It is clear from the figure that the experimental depth

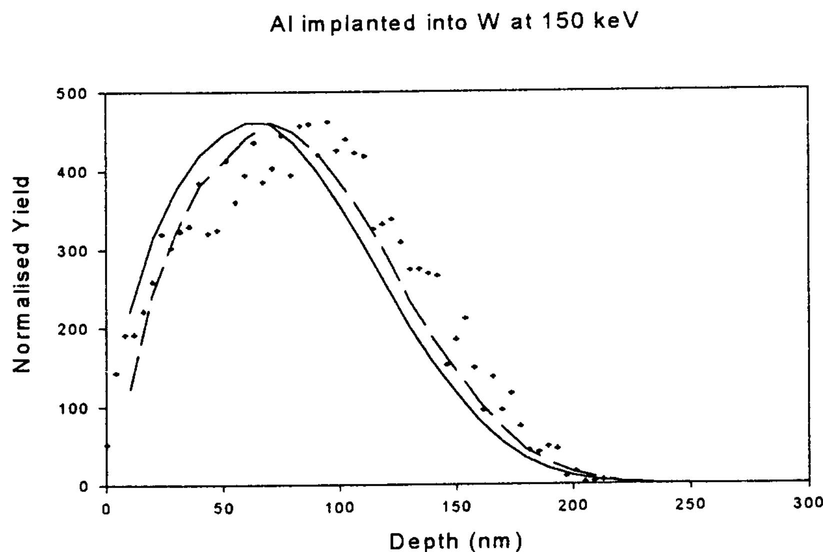


**Figure 6.8:** Experimental aluminium profiles(symbols) in tungsten for an implantation dose of 5 x $10^{16}$ $Al^+$ $cm^{-2}$ at 150 keV compared with TRIM-95 before(dashes) and after(solid line) taking sputtering into account.

distribution disagrees with TRIM-95 predictions. The experimentally determined first range moment was 10% larger than the theoretical predictions which is also outside the experimental error. The second range moment obtained experimentally was found to be 8% larger than the theoretical value.

### 6.1.9 ALUMINUIM IMPLANTED INTO HAFNIUM

The depth distribution for aluminium implanted into hafnium sample is depicted in figure 6.9. From this it is evident that there is a poor agreement between the experimental and theoretical profiles. When comparing the range moments of the depth distributions, one finds that the experimentally determined projected range moment is 14% larger than the theoretical

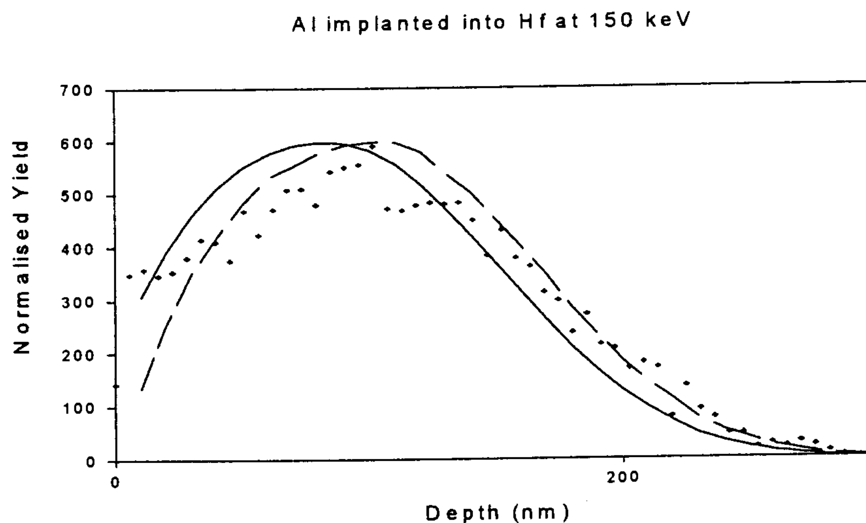


**Figure 6. 9:** Experimental aluminium profiles(symbols) in hafnium for implantation fluence of 5 x $10^{16}$ $Al^{+}$ $cm^{-2}$ at 150 keV compared with TRIM-95 predictions before(dashes) and after(solid line) taking sputtering into account

predictions which is far outside the experimental error. The straggling width obtained experimentally was also found to be 16% larger than the value predicted by TRIM-95. This large discrepancy is outside the experimental error.

## 6.2 COMPARISON WITH RESULTS IN THE LITERATURE

The experimentally determined range moments for vanadium, chromium, cobalt, yttriumm, and platinum targets agree very well with TRIM predictions, while the values for tungsten are just outside the experimental error. However, serious disagreement is found for manganese, tantalum and hafnium targets. The first two metals have significantly lower projected ranges and straggling widths, while for hafnium both moments are appreciably higher than predicted. Keinonen et al [5] presented average projected ranges about 38% larger than expected for 100 keV aluminium ions implanted in metals having similar atomic numbers than investigated in this work.

However, they obtained this figure by comparing their results with LSS calculations using the Thomas-Fermi potential. By analyzing their results using TRIM simulations, their average projected range is found to be only 17 % larger, while our values at 150 keV are on average in good agreement with these predictions. Comparing specific metals, the results for tantalum display the worst disagreement: we obtained values for the first two range moments, which are 18% smaller than obtained with TRIM simulations,

while reference [5] determined a projected range about 17% larger than this estimate. Slightly better agreement is found for tungsten, where our and their experimental projected range are 11% and 25% higher than the theoretical values respectively. Range parameters of 150 keV energy aluminium ions implanted in six metals with atomic numbers in the range of $12 \leq Z_2 \leq 42$ are on average about 7% lower than predicted by TRIM [7], which is more or less compatible with the expected experimental error and the results of this work.

## 6.3 CONCLUSION

The shape of the aluminium distributions agree within experimental uncertainty with a gaussian distribution, although the large relative errors calculated for the higher moments make any meaningful analysis impossible. For heavier metals ($Z_2 \geq 30$) sputtering effects modify the aluminium implantation profiles considerably for fluence in the $10^{16}$ $cm^{-2}$ range, although for the metals investigated in this work only the first range moments were affected significantly and could be corrected by simply multiplying them with a sputter correction factor. This might not be sufficient for metals with low melting points and consequently high sputter coefficients like for example tin, gold, and lead. In those cases a more involved correction procedure will have to be applied.

# REFERENCES

1. P.D. Townsend, J.C. Kelly, N.E.W. Hartley, *Ion Implantation, Sputtering and their Application*, Academic Press, (1976) 111-126.
2. M. Hayes, E. Friedland, S. Kalbitzer, B. Hartman and S. Fabian, in: *Ion Beam Modification of Materials, 9th International Conference*, ed. J.S. Williams, R.G. Elliman and M.C. Ridgway North-Holland, (1996) 698.
3. H. Ryssel and I. Ruge, *Ion Implantation*, John Wiley & Sons, (1986) 10-12, 19.
4. M. Behar, P.F.P Fichtner, P.L Grande, F.C Zawislak, Material Science and Engineering R15, Nos. 1-2 July, (1995) 1-83
5. J. Keinonen, M. Hautala M. Loumajarvi M. Bister, A. Anttila, Rad. Effects 39 (1978) 189.
6. M.R. Herberts, P.F.P. Fichtner and M. Behar, Nucl. Instr. and Meth. B111 (1996) 12.
7. M. Hayes, E. Friedland, T. Hauser, Mat. Sci. Forum 248 (1996) 107.
8. C. Endt and P.M. van der Leun, Nuclear Physics A214, (1973).
9. Robert F. Hochman, *Ion plating and implantation*, American Society for metals, (1985) 8-9, 10.
10. J.W. Mayer, L.C. Feldman, *Fundamental of Surface and Thin Film Analysis*, North-Holland, New York, (1986) 74-80.
11. J. Lindhard, A. Winter, Kgl. Danske Videnskab. Selskab, Mat.-Fys. Medd 34, no. 4, (1964).
12. H.H. Anderson and J.F. Ziegler, *The Stopping and Ranges of Ions in Matter*, vol. 3, edited by J.F. Ziegler, Pergamon, New York, (1977).
13. J.F. Ziegler, J.P. Biersack and U. Littmark, in: *Stopping and Ranges of Ions in Solid*, vol.1, ed. J.F. Ziegler, Pergamon, New York, (1985).